Texture-adaptive mother wavelet selection for texture analysis

Chrarith Abhayaratne, Ian Jermyn, Josiane Zerubia

INSTITUT NATIONAL DE RECHERCHE EN INFORMATIQUE ET EN AUTOMATIQUE

Texture-adaptive mother wavelet selection for texture analysis

G. C. K. Abhayaratne — Ian Jermyn — Josiane Zerubia

N°8783

December 2003

THÈME 3

ISSN 0249-6399

Texture-adaptive mother wavelet selection for texture analysis

G. C. K. Abhayaratne *, Ian Jermyn , Josiane Zerubia

Thème 3 — Interaction homme-machine,
images, données, connaissances
Projets Ariana

Rapport de recherche n°8783 — December 2003 — 25 pages

Abstract: We discuss the use of texture-adaptive mother wavelets in an adaptive probabilistic wavelet packet approach to texture analysis. First, we present the use of adaptive biorthogonal wavelet packet bases in such an analysis, thus combining the advantages of biorthogonal wavelets (FIR, linear phase) with those of a coherent texture model. In this case, the computation of the probability uses both the primal and dual coefficient of the adapted biorthogonal wavelet packet basis. The computation of the biorthogonal wavelet packet coefficient is done using a lifting scheme, which is very efficien in terms of reducing the computational complexity and achieving an intrinsic parameterization of wavelet filters Then we include the mother wavelet parameter into this model, in order to fin the optimal mother wavelet for a given texture using this model. The model is applied to the classificatio of mosaics of Brodatz textures, the results showing improvement over the performance of the corresponding orthogonal wavelets.

Key-words: texture classification orthogonal wavelets, biorthogonal wavelets, texture-adaptive mother wavelets, lifting, wavelet packets.

* The work of Dr. Abhayaratne was funded by the ERCIM postdoctoral fellowship programme.

Unité de recherche INRIA Sophia Antipolis
2004, route des Lucioles, BP 93, 06902 Sophia Antipolis Cedex (France)
Téléphone : +33 4 92 38 77 77 — Télécopie : +33 4 92 38 77 65

Résumé : Pas de résumé

Mots-clés : calcul formel, base de formules, protocole, différentiation automatique, génération de code, modélisation, lien symbolique/numérique, matrice structurée, résolution de systèmes polynomiaux, géométrie effective

Contents

1 Introduction **4**

2 Biorthogonal Wavelet Transforms and The Lifting Scheme **6**
2.1 The Lifting Scheme 6
2.2 Biorthogonal Wavelets Using Lifting 8

3 Adaptive Biorthogonal Wavelet Packets for Texture Analysis **10**
3.1 Texture Model 10
3.2 Parameter Estimation 11
3.3 Classif cation 12
3.4 Experimental Results 12
3.4.1 Parameter Estimation 12
3.4.2 Classif cation 14
3.5 Conclusions 16

4 Optimal Mother Wavelet Selection for Texture Analysis **17**
4.1 Texture Model 17
4.1.1 Parameter Estimation 17
4.1.2 Classif cation 18
4.2 Experimental Results 18
4.2.1 Parameter Estimation 18
4.2.2 Classif cation 20
4.3 Conclusions 22

5 Conclusions **23**

1 Introduction

The segmentation and classif cation of images based on texture analysis plays a major role in image understanding applications. Over the years, texture analysis has received considerable attention in terms of both methodology and application. The commonly used methods are based on statistical, model-based, and signal processing features.

In the signal processing approaches for texture analysis, feature extraction mainly includes two steps: the signal decorrelation step which usually consists of a f lter or a signal transform and the computation of the feature metric, which is either an energy or a probability measure. The frequency domain energy distributions produced by signal transforms are used for the extraction of texture features. The commonly used transforms for texture analysis include Gabor transforms [1, 2], ring and wedge transforms [3], wavelet transforms as wavelet packet decomposition [4, 5, 6, 7, 8, 9] or as wavelet frame decomposition [10, 11, 12], which is an over-complete representation. For a comparative study on above techniques, see [13].

Wavelets-based approaches for texture analysis usually employ a single mother wavelet f xed for all textures. In these schemes only the wavelet packet tree of the optimum subband decomposition, and the statistical properties, such as, mean and variance, associated with the marginal densities of its wavelet subband coeff cients are used as features of the texture model. However, [6, 7] noted that the optimal tree for a given texture, and classif cation performance, both vary according to the mother wavelet used in the texture model. Previous studies have also shown that the length, number of vanishing moments, regularity, orthogonality, and degree of the impulse response shift variance of the mother wavelet contribute to the results of wavelet based applications such as image coding [14] and texture analysis [15]. Therefore, an optimal choice of a mother wavelet for the representation of a given texture can be used in feature extraction for a given texture. With a similar point of view, in f lters based methods, where a f lter and a response energy measure is used as the feature extractor, optimization of f lters has been used in order to achieve optimized energy separation [16, 17, 18].

Another noticeable feature of work on wavelet-based texture analysis is that it has focused only on orthogonal wavelets, which have the drawback that their design constraints do not allow the wavelet f lter to be both FIR and linear phase, *i.e.,* both real and symmetric. This can, however, be achieved for biorthogonal wavelets, where the analysis (primal) wavelet and the synthesis (dual) wavelet differ in length. It is well known that biorthogonal wavelets outperform orthogonal wavelets in image coding [19].

The main aim of this report is to discuss the f rst steps toward texture-adaptive mother wavelet selection for texture analysis by modifying the texture analysis approach presented in [6]. We present two additions to the model: modif cations to use biorthogonal wavelets, and modif cations to incorporate the optimal mother wavelet. We also use the lifting factorization [20, 21] of wavelet transforms in this model, since it forms a natural parameterization of the corresponding wavelet f lter banks, that can be used in the mother wavelet optimization. The lifting scheme also enables fast computation, in both training and classif cation.

The rest of the report is organized as follows: In section 2, we present the basics of the lifting scheme and introduce the lifting factorization of the class of biorthogonal wavelets to be used in the texture model. In section 3, we modify the approach to texture analysis presented in [6] to use

biorthogonal wavelets. In section 4, we present the optimal selection of mother wavelets for texture analysis using the adaptive biorthogonal wavelet packet model in section 3. In both sections, we demonstrate the performance of these resulting models in texture classif cation experiments using Brodatz textures. Section 5 shows conclusions and our future work on texture-adaptive mother wavelet selection for texture classif cation.

2 Biorthogonal Wavelet Transforms and The Lifting Scheme

The wavelets are localized waves. Once the "mother wavelet" $\Phi(t)$, which is a zero mean function, is def ned, it is dilated and translated to obtain a family of wavelets $\Phi_{(a,b)}(t)$ corresponding to the scale a and and the position b, which can be def ned as follows [22, 23]:

$$\Phi_{(a,b)}(t) = \frac{1}{\sqrt{a}}\,\Phi\left(\frac{t-b}{a}\right) \tag{1}$$

The set of functions obtained by the mother wavelet forms a basis for signal representation. Thus, any f nite energy signal can be represented as a linear combination of the wavelets $\Phi_{(a,b)}(t)$. The wavelet coeff cients $f_{(a,b)}$ of an input signal $f(t)$ are def ned as:

$$f_{(a,b)} = \int_{-\infty}^{\infty} \Phi_{(a,b)}(t)\, f(t)\, dt. \tag{2}$$

In the discrete wavelet transform (DWT), the mother wavelet is dilated and translated by discrete values, in most cases by a power of two (dyadic) dilations. An example is shown below.

$$\Phi_{(a,b)}(t) = 2^{a/2}\,\Phi(2^a t - b) \tag{3}$$

2.1 The Lifting Scheme

There are two approaches for realizing the DWT: f lter banks and lifting. The f lter bank approach uses two f lter banks, one each for the analysis (forward transform) and the synthesis (inverse transform. In a 2-band wavelet decomposition, the analysis f lter bank consists of a high pass f lter that corresponds to detailing the input signal with the wavelet $\Phi_{(a,b)}(t)$ and a low pass f lter that corresponds to averaging the input signal with the corresponding scaling function. Both f lters in the analysis f lter bank are followed by a factor 2 down-sampling f lter.

The second approach is the lifting scheme [20, 21, 24]. The idea of lifting was originated as a method of building the second generation wavelets, where the wavelets are not necessarily translates and dilates of the mother wavelet as in the f rst generation wavelets. The f rst generation wavelets were constructed with the aid of Fourier transform techniques. But construction of wavelets using the lifting approach does not require Fourier transform techniques as lifting is entirely a spatial method. It also forms a natural parameterization of the corresponding f lter banks for spatial domain design and implementation. In addition, lifting also yields in-place computation of the wavelet transform coeff cients, thus enabling fast and memory eff cient computations.

The basic idea of lifting is the factorization of the polyphase matrix of the f lter bank for a given wavelet transform into alternating upper and lower triangular matrices with unit diagonals using the Euclidean factoring algorithm [20].

We demonstrate the f lter bank and lifting relationship for a 2-band wavelet transform, as below. Let H be the low pass f lter of length $(m1+\,m2+1)$ in the wavelet f lter bank with coeff cients:

$$(h_{-m1}, \ldots, h_{-1}, h_0, h_1, \ldots, h_{m2}),\ \text{where}\ \sum_{k=-m1}^{m2} h_k = 1.$$

Similarly, let F be the high pass f lter of length ($l1$+$l2$+1) in the wavelet f lter bank with coeff cients:

$$(f_{-l1}, \ldots, f_{-1}, f_0, f_1, \ldots, f_{l2}), \text{ where } \sum_{k=-l1}^{l2} f_k = 0.$$

Following the z-transform domain def nition of the polyphase components, $x_e(z)$ and $x_o(z)$ of a 1D signal X:

$$x(z) = x_e(z^2) + zx_o(z^2), \tag{4}$$

where $x_e(z) = \sum_k x_{2k} z^{-k}$ and $x_0(z) = \sum_k x_{2k+1} z^{-k}$, we def ne the polyphase matrix $M(z)$ of the wavelet f lter bank as follows:

$$\begin{pmatrix} h_e(z) & h_o(z) \\ f_e(z) & f_o(z) \end{pmatrix}.$$

It is customarily to normalize the wavelet coeff cients. In f lter banks, this is achieved by multiplying the output of H and G by $\sqrt{2}$ and $1/\sqrt{2}$, respectively [22].

The f rst step of the classical lifting realization of a 1D wavelet transform is splitting the input x^0 into its polyphase components, even indexed samples ($x(z)$) and odd indexed samples ($y(z)$) using the relationship in (4). The splitting for an input signal x^0 is:

$$\text{Split:} \quad x_i = x^0_{2i}; \quad y_i = x^0_{2i+1} \tag{5}$$

Then the lifting steps are def ned by the factorization of the corresponding polyphase matrix into alternating unit diagonal lower and upper matrices, also known as elementary matrices. For the simplest case, there can be at least two such matrices def ning two lifting steps: Prediction lifting (P) and Update lifting (U) steps corresponding to the predictor $P(z)$ and the update function $U(z)$, respectively. Prediction and update lifting steps are def ned as follows:

$$\text{Prediction :} \quad y'(z) = \quad y(z) - P(z)x(z) \tag{6}$$

$$\text{Update :} \quad x'(z) = \quad x(z) + U(z)y'(z) \tag{7}$$

Usually, these three lifting steps are followed by a normalization step with normalization constants K_e and K_o, where $K_e = \sqrt{2}/(|\sum h_e| + |\sum h_o|)$ and $K_o = \sqrt{2}/(|\sum f_e| + |\sum f_o|)$.

$$\text{Normalize:} \quad x''_i = K_e x'_i; \quad y''_i = K_o y'_i \tag{8}$$

The above four lifting steps in matrix form is formulated as below:

$$\begin{bmatrix} x'' \\ y'' \end{bmatrix} = \underbrace{\begin{bmatrix} K_e & 0 \\ 0 & K_o \end{bmatrix}}_{\mathbf{K}} \underbrace{\begin{bmatrix} 1 & U(z) \\ 0 & 1 \end{bmatrix}}_{\mathbf{U}} \underbrace{\begin{bmatrix} 1 & 0 \\ -P(z) & 1 \end{bmatrix}}_{\mathbf{P}} \begin{bmatrix} x \\ y \end{bmatrix} \tag{9}$$

The product matrix $\mathbf{KUP}$ is the polyphase matrix of the corresponding f lter bank.

For the wavelet transforms based on a single P-U lifting step, we can rewrite the lifting in (6) and (7) as follows:

$$\text{Prediction :} \quad y'(z) = \quad y(z) - P^i(z)x(z) \tag{10}$$

$$\text{Update :} \quad x'(z) = \quad x(z) + \frac{1}{2}U^i(z)y'(z) \tag{11}$$

where the prediction (P^i) and update (U^i) functions are weighted averaging operators, with the sum of weights equals to 1. When both P^i and U^i are interpolating functions, this scheme leads to generating the class of wavelets known as *interpolating wavelets* [21]. For example, using $P^i(z) = U^i(z) = 1$, *i.e.,* the left/right neighbour interpolating functions, with the normalization constants $\{K_e, K_o\} = \{\sqrt{2}, \frac{1}{\sqrt{2}}\}$, yields the Haar wavelet transform.

2.2 Biorthogonal Wavelets Using Lifting

Let $|a\rangle$ and $|s\rangle$ be the primal and dual wavelet of a wavelet transform, respectively. We use only a single prediction-update lifting step pair to obtain the wavelet decomposition of the primal wavelet $|a\rangle$. Thus, the primal wavelet transform is obtained using P+U lifting:

$$\text{P}: \quad y'_i = \quad y_i - \sum\nolimits_{j=1-\lceil M/2 \rceil}^{\lfloor M/2 \rfloor} p_j x_{j+i} \tag{12}$$

$$\text{U}: \quad x'_i = \quad x_i + \frac{1}{2} \sum\nolimits_{j=-\lfloor \tilde{M}/2 \rfloor}^{\lceil \tilde{M}/2 \rceil - 1} u_j y'_{j+i} \tag{13}$$

$$\text{Normalize}: \quad x''_i = \quad \sqrt{2} x'_i; \quad y''_i = y'_i / \sqrt{2} \tag{14}$$

where $\sum_j p_j = \sum_j u_j = 1$; M and $\tilde{M}$ are the number of vanishing moments in the prediction and update polynomials, respectively.

From (9) and the above lifting steps, we can write the corresponding polyphase matrix for the $|a\rangle$ as follows:

$$M_{|a\rangle}(z) \quad = \quad \begin{bmatrix} K_e \left(1 - \frac{1}{2} P(z) U(z)\right) & K_e \frac{1}{2} U(z) \\ -K_o P(z) & K_o \end{bmatrix}, \tag{15}$$

We recall the perfect reconstruction (PR) conditions for biorthogonal wavelets:

$$H_s(z) = F_a(-z) \text{ and } F_s(z) = -H_a(-z), \tag{16}$$

where H and F refer to low and high pass f lters, respectively and the subscripts a and s denote the analysis (with the primal wavelet) and synthesis (with the dual wavelet) f lter banks, respectively. By considering the PR condition, and the corresponding sampling pattern in the synthesis wavelet we can write the polyphase matrix for the dual wavelet $|s\rangle$ as follows:

$$M_{|s\rangle}(z) \quad = \quad \begin{bmatrix} K_o & K_o P(z) \\ -K_e \frac{1}{2} U(z) & K_e \left(1 - \frac{1}{2} P(z) U(z)\right) \end{bmatrix}, \tag{17}$$

which leads to the following factorization:

$$M_{|s\rangle}(z) = \underbrace{\begin{bmatrix} K_o & 0 \\ 0 & K_e \end{bmatrix}}_{\mathbf{K}} \underbrace{\begin{bmatrix} 1 & 0 \\ -\frac{1}{2} U(z) & 1 \end{bmatrix}}_{\mathbf{P}} \underbrace{\begin{bmatrix} 1 & P(z) \\ 0 & 1 \end{bmatrix}}_{\mathbf{U}} \tag{18}$$

Thus, the dual wavelet $|s\rangle$ is obtained using U+P lifting:

$$\text{U}: \quad x'_i = \quad x_i + \sum_{j=1-\lceil M/2 \rceil}^{\lfloor M/2 \rfloor} p_j y_{j+i} \tag{19}$$

$$\text{P}: \quad y'_i = \quad y_i - \frac{1}{2} \sum_{j=-\lfloor \tilde{M}/2 \rfloor}^{\lceil \tilde{M}/2 \rceil - 1} u_j x'_{j+i} \tag{20}$$

$$\text{Normalize}: \quad x''_i = \quad x'_i/\sqrt{2}; \quad y''_i = \sqrt{2} y'_i \tag{21}$$

Such wavelet pairs are usually denoted as $(M, \tilde{M})$, where M ($\tilde{M}$) is the number of vanishing moments in the $|a\rangle$ ($|s\rangle$) mother wavelet.

We conclude this section with some relationships that will be used in the derivations in the following sections.

The PR property: Let ϕ be an input signal. Then,

$$|\phi\rangle = \sum_i |a\rangle\langle s|\phi\rangle = \sum_i |s\rangle\langle a|\phi\rangle. \tag{22}$$

Thus,

$$\sum_i |a\rangle\langle s| = \sum_i |s\rangle\langle a| = I, \tag{23}$$

where I is the Identity operator.

The wavelet coeff cients w_{a_i} and w_{s_i} at position i using the $|a\rangle$ and $|s\rangle$, respectively are follows:

$$w_{a_i} = \sum_i \langle \phi | a_i \rangle \tag{24}$$

$$w_{s_i} = \sum_i \langle \phi | s_i \rangle \tag{25}$$

For the orthogonal wavelets, $w_{a_i} = w_{s_i}$, which is not true for biorthogonal wavelets, since $M_a(z) \neq M_s(z)$.

Finally, we def ne the energy in the wavelet domain $E(\phi)$ as follows:

$$\begin{aligned} E(\phi) &= \langle \phi | \phi \rangle \\ &= \sum_i \langle \phi | s \rangle \langle a | \phi \rangle \\ &= \sum_i w_{a_i} w_{s_i} \end{aligned} \tag{26}$$

3 Adaptive Biorthogonal Wavelet Packets for Texture Analysis

In this section, we modify the approach to texture analysis presented in [6] to use biorthogonal wavelets, and then demonstrate their performance in texture classif cation experiments using Brodatz textures. In section 3.1, we describe the adaptive probabilistic texture model using biorthogonal wavelets. Section 3.4 shows the results of parameter estimation, and the classif cation of mosaics using Brodatz [25] textures, followed by the conclusions about adaptive biorthogonal wavelet packets for texture analysis in section 3.5.

3.1 Texture Model

The purpose of this section is to review the model described in [6] and to adapt it to use biorthogonal wavelets.

The model in [6] starts from a general translation invariant Gaussian distribution. The marginalized Gaussian distribution on an image region is then derived, and shown to be tractable if the original covariance lies in a certain class of operators. This class consists of those operators that are diagonal in at least one wavelet packet basis. The model is thus parameterized by a dyadic partition of the Fourier domain, which in conjunction with a mother wavelet def nes a wavelet packet basis, and a function that assigns to each element of the partition (*i.e.,* each subband), its variance. In [6], it is shown that exact maximum a posteriori (MAP) estimates of these parameters can be learned from samples of a texture using an eff cient depth-f rst search algorithm on the space of dyadic partitions. The result is a model in which the basis adapts to the structure inherent in the texture according to a criterion derived from the texture model itself, rather than introduced on an *ad hoc* basis.

The Gaussian assumption might appear to go against the fact that the subband histograms of standard wavelet coeff cients take on a leptokurtotic form more closely modelled by, for example, a generalized Gaussian with shape factor less than unity. However, most of these studies were concerned with 'natural' images. The statistics were thus comprised of mixtures of many components corresponding to different entities in the scene. There is no reason to suppose that these statistics will be preserved for the images in a coherent texture class. Second, products of generalized Gaussians do not preserve their form under a change of basis, so that in a basis adapted to the texture class under consideration, again there is no reason to suppose that the statistics will necessarily assume the standard form. In the absence of more specif c information, a Gaussian distribution is used as a maximum entropy choice: it supposes only that the energy in each of the adaptive subbands will be approximately preserved from texture sample to texture sample.

Following the line of argument used in [6], we can derive the expression for the model in terms of biorthogonal wavelets as follows:
We start with the marginalized Gaussian distribution for the image I_R on an image region R:

$$\Pr(I_R|\cdot) = |G_R/\pi|^{1/2} e^{-\langle\phi|G_R|\phi\rangle}, \tag{27}$$

where G_R is an operator derived from the inverse covariance operator F [7]. Using the biorthogonal bases $|a\rangle$ and $|s\rangle$, we can write:

$$\begin{aligned}\langle\phi|G_R|\phi\rangle &= \sum_{i,j}\langle\phi|a_i\rangle\langle s_i|G_R|a_j\rangle\langle s_j|\phi\rangle \\ &= \sum_i \langle\phi|a_i\rangle f_i \langle s_i|\phi\rangle \\ &= \sum_i w_{a_i} f_i w_{s_i}. \end{aligned} \tag{28}$$

At the same time, we can show that the operator G_R is diagonal in the Fourier domain, which is a requirement for satisfying the translational invariance property of the probability measure, as follows:

$$\begin{aligned}G_R(k,k') = \langle k|G_R|k'\rangle &= \sum_i \langle k|a_i\rangle f_i \langle s_i|k'\rangle \\ &= f(k)\sum_i \langle k|a_i\rangle\langle s_i|k'\rangle \\ &= f(k)\delta(k,k'). \end{aligned} \tag{29}$$

Thus, the biorthogonal wavelet model is still characterized by a dyadic partition T and a function f on the partition, but now the probability distribution is given by:

$$\Pr(I|f,T) = \prod_{\alpha\in T}\left[\left(\frac{f_\alpha}{\pi}\right)^{\frac{N_\alpha}{2}} e^{-f_\alpha \sum_{i\in\alpha} w_{a_{\alpha,i}} w_{s_{\alpha,i}}}\right] \tag{30}$$

where I is the image; α indexes the subbands of T; f_α is the value of f on subband α; i indexes the wavelets within each subband; $w_{a_{i,\alpha}}$ and $w_{s_{i,\alpha}}$ are the (α, i) coeff cients using the wavelet bases from the primal ($|a\rangle$) and dual ($|s\rangle$) wavelets, respectively; and N_α is the number of pixels in the subband α.

The model we derived for biorthogonal wavelets reduces to that for orthogonal wavelets, as in [6], when the primal and dual bases are the same ($|a\rangle = |s\rangle$); thus we can use this model for orthogonal wavelets too.

3.2 Parameter Estimation

MAP estimates of the parameters for a given texture are found by examining the probability of the parameters given a set of images $d = \{I_n\}$ of the texture:

$$\Pr(f,T|d) \propto \Pr(d|f,T)\Pr(f|T)\Pr(T) \tag{31}$$

We choose $\Pr(f|T)$ to be Jeffrey's ignorance prior. We choose the probability of a given partition T to be $\Pr(T) = Z^{-1}(\beta)e^{-\beta\sum_{t\in Q(T)} N_t}$ where $Q(T)$ is the quadtree naturally related to the partition,

t is a vertex in this tree, and $N_t \propto 4^{-l(t)}$, where $l(t)$ is the depth of vertex t in the tree, is the size of the region of the Fourier domain corresponding to vertex t. The parameter β controls how severely the distribution penalizes large decompositions. Differentiating (30) with respect to f_α gives us the MAP estimate of f for a fixed T:

$$\hat{f}_\alpha = \frac{N_\alpha}{2\sum_{i\in\alpha} |w_{a_{i,\alpha}} w_{s_{i,\alpha}}|} \tag{32}$$

A depth-first search through the space of dyadic decompositions allows us to find the MAP estimate for T efficiently.

3.3 Classification

In order to classify pixels, we use an undecimated wavelet decomposition, and consider the following approximation to the exact probability distribution for the texture on a region R:

$$\Pr(I_R|f,T) = \prod_{\alpha\in T}\prod_{x\in R}\left[\left(\frac{f_\alpha}{\pi}\right)^{\frac{1}{2M_\alpha}} e^{-\frac{f_\alpha}{M_\alpha}\sum_{i\in\alpha} w_{a_{\alpha,x}} w_{s_{\alpha,x}}}\right] \tag{33}$$

where $M_\alpha = 4^{l(\alpha)}$ is the redundancy factor for subband α in the undecimated transform. The class of a pixel, $\lambda(x)$, is then estimated as:

$$\hat{\lambda}(x) = \arg\max_{l\in L} \Pr(I_{V(x)}|\lambda_{V(x)} = l) \tag{34}$$

where $V(x)$ is a set of neighbours of pixel x.

3.4 Experimental Results

We present the performance of biorthogonal wavelets with vanishing moments (2,2), (4,2), (4,4), and (2,4), and compare them with orthogonal wavelets Haar, D4, and D8, which are the compact support wavelets with 1, 2, and 4 vanishing moments respectively. Table 1 summarizes the details of the wavelets used in these simulations, where : l_a is the length of the primal mother wavelet and l_s the length of the dual mother wavelet. The top part of the table shows the biorthogonal wavelets, while the bottom part shows the orthogonal wavelets. The biorthogonal wavelet (2,2) and the orthogonal wavelet D4 contain the same number of vanishing moments in the wavelets but differ only in terms of the lengths of those wavelets. A similar relationship can be seen between (4,4) and D8 wavelets.

3.4.1 Parameter Estimation

The parameters T and f are estimated as described earlier. They are shown graphically in figure 1 for four textures: Raffia, Herring, Wool, and Grass; and two wavelets: (2,2) and (4,2). The brightness of each subband is proportional to $1/f_\alpha$.

	M	$\tilde{M}$	l_a	l_s
(2,2)	2	2	3	5
(2,4)	2	4	3	9
(4,2)	4	2	7	9
(4,4)	4	4	7	13
Haar	1	1	2	2
D4	2	2	4	4
D8	4	4	8	8

Table 1: The biorthogonal and orthogonal wavelets used in the experiments. M ($\tilde{M}$) is the number vanishing moments and l_a (l_s) is the length of the primal (dual) mother wavelet.

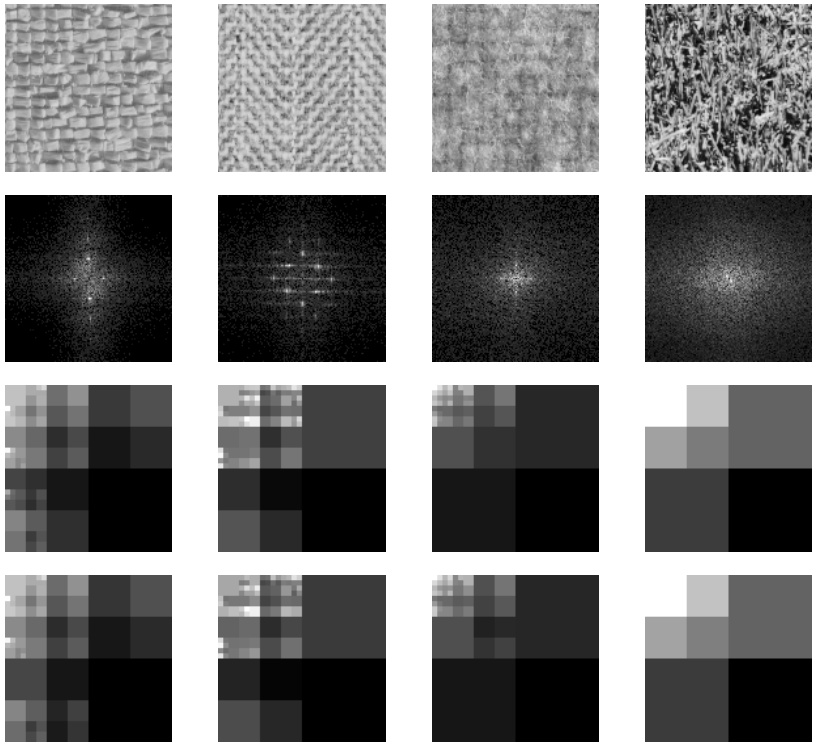

Figure 1: Parameter estimation. Row 1: textures Raffia, Herring, Wool, and Grass; row 2: their power spectra; rows 3-4: their estimated parameters using (2,2) and (4,2) wavelets.

3.4.2 Classif cation

We present the classif cation performance of the biorthogonal wavelet model using single texture images and mosaic images of Brodatz textures. Figure 2 shows the classif cation maps for four textures, classif ed using all four trained texture models on each of the single texture images. It shows the test textures, the corresponding ground truth maps, and the classif cation results. The percentages of misclassif ed pixels are listed in table 2.

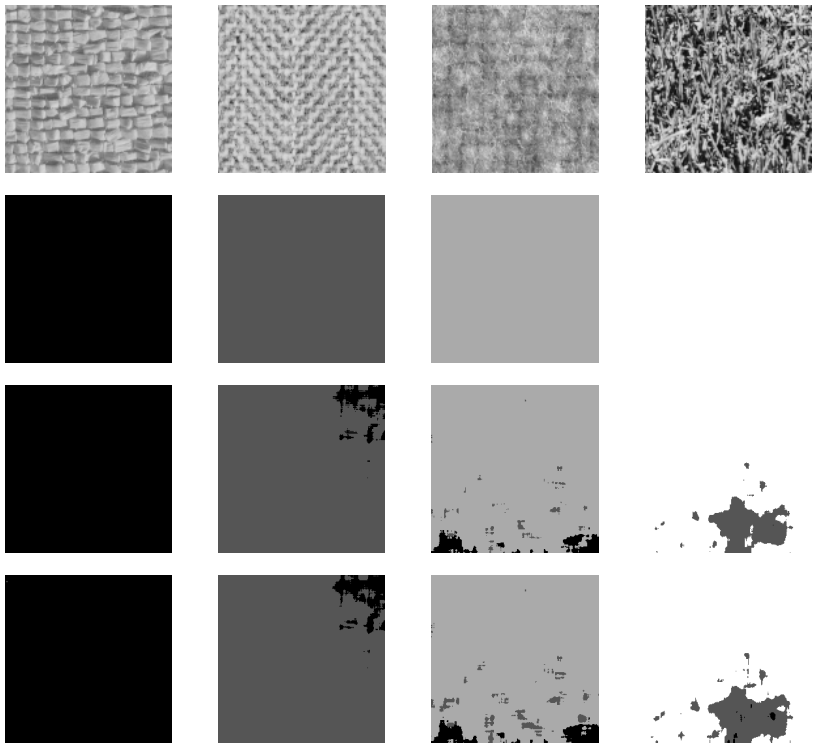

Figure 2: Classif cation results. Row 1: single texture images; row 2: ground truth; rows 3-4: classif cations using (2,2) and (4,2) wavelets.

Similarly, in f gure 3, we show the test mosaics, M1, M2, M3 and M4, the corresponding ground truth maps, and the misclassif cation maps, where the misclassif ed pixels are shown in black, for two different biorthogonal wavelets: (2,2) and (4,2).

The percentages of misclassif ed pixels are listed in table 3. It is evident from these results that for both orthogonal and biorthogonal wavelets, shorter mother wavelets with a smaller number of vanishing moments outperform longer mother wavelets with a larger number of vanishing moments. Moreover, we can compare the performance of the biorthogonal wavelet (2,2) with that of the or-

	T1	T2	T3	T4	Average
(2,2)	0.00	3.86	4.89	9.76	4.63
(2,4)	0.19	1.79	13.11	11.91	6.75
(4,2)	0.01	4.80	7.16	11.97	5.98
(4,4)	0.18	1.89	15.49	10.02	6.90
Haar	0.01	1.82	2.42	1.28	1.40
D4	0.37	0.26	31.34	0.03	8.00
D8	0.22	1.45	36.49	0	9.54

Table 2: Percentages of misclassif ed pixels (single textures).

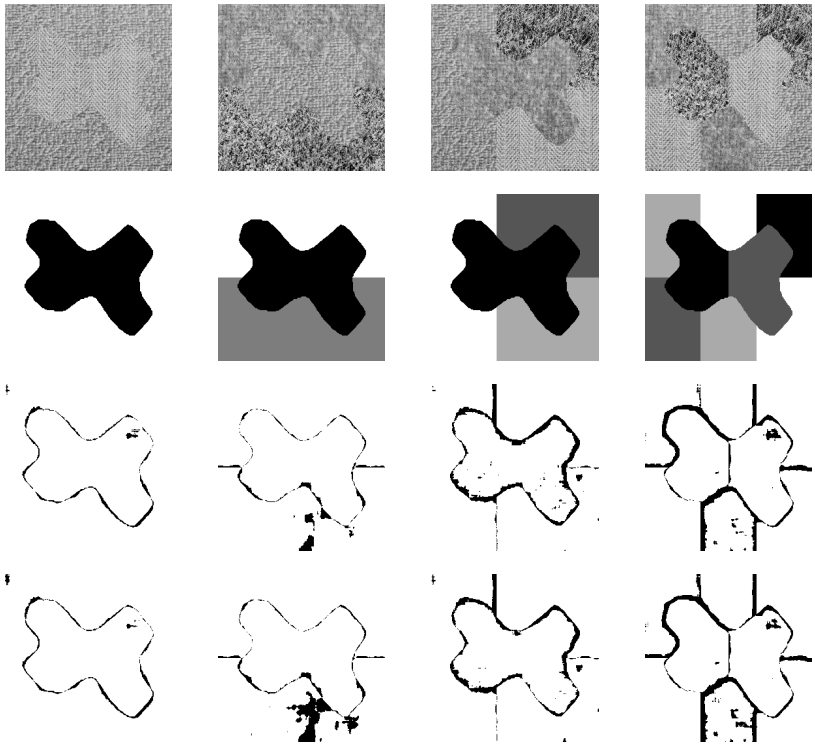

Figure 3: Classif cation results. Row 1: mosaics M1, M2, M3, and M4; row 2: ground truth; rows 3-4: misclassif ed pixels (in black) for classif cations using (2,2) and (4,2) wavelets.

thogonal wavelet D4, since they have the same number of vanishing moments in both primal and

	M1	M2	M3	M4	Average
(2,2)	2.64	3.33	6.74	8.63	5.33
(2,4)	2.67	4.72	6.78	10.96	6.28
(4,2)	2.83	5.77	6.06	9.18	5.96
(4,4)	2.83	7.60	6.07	10.62	6.78
Haar	2.18	2.53	6.16	8.86	4.93
D4	6.58	2.18	29.34	20.34	14.61
D8	4.63	3.38	22.03	24.11	13.54

Table 3: Percentages of misclassif ed pixels (mosaics).

dual wavelets (2 each), and they are the compact support wavelets for that vanishing moment pair in orthogonal and biorthogonal wavelets, respectively. As can be seen in table 3, the (2,2) wavelet outperforms the D4 wavelet for the mosaics: M1, M3 and M4, and on average for the three mosaics. Similar performance can be seen for the biorthogonal and orthogonal wavelets with 4 vanishing moments, (4,4) and D8.

3.5 Conclusions

In this section, we have presented an adaptive probabilistic texture model based on biorthogonal wavelets, and used it for texture classif cation and analysis. In this model, both the primal and the dual wavelets associated with a specif c biorthogonal wavelet transform are used in the energy computation, in parameter estimation, and for classif cation. For both orthogonal and biorthogonal wavelets, shorter wavelets with fewer vanishing moments classify better than longer wavelets with more vanishing moments. The biorthogonal wavelets (2,2) and (4,4) resulted in better classif cations compared to the corresponding compactly supported orthogonal wavelets with the same number of vanishing moments, D4 and D8.

4 Optimal Mother Wavelet Selection for Texture Analysis

It is evident from the classif cation results shown in the previous section, that no single wavelet has resulted in the lowest classif cation errors for all the test mosaics. For example, (4,2) and (2,2) wavelets yielded the best classif cation for the mosaics M3 and M4, respectively, while the Haar wavelet resulted in the best performance for M1 and M2. Not only the classif cation results, but also the tree partition for a trained texture also varies with the mother wavelet used in training as can been seen from Figure 1. These observations imply that the mother wavelet used in training the texture model would be used as a parameter of the texture model, if the texture model was optimized by varying the mother wavelet used in the texture model.

The main objective of this section is to incorporate the mother wavelet f lter parameters into the texture model presented in section 3.1 and to investigate the effect of that in texture classif cation. In this report, we only focus on f nding an optimal mother wavelet for the texture model of a given texture by considering only a f nite set of mother wavelet choices. In section 4.1, we present the new texture model and discuss the parameter estimation and classif cation. In section 4.2, we show the parameter estimation and classif cation performances of the new texture model using the same textures and mosaics used in the previous section, followed by the conclusions in section 4.3.

4.1 Texture Model

In this case, we start with the biorthogonal wavelet texture model in (30), which is characterized by a dyadic partition T and a function f on the partition, and include the mother wavelet W, where $W = (p, u)$ is the choice for the weights of the lifting steps that def ne the primal ($|a\rangle$) and dual ($|s\rangle$) wavelets, as follows:

$$\Pr(I|f,T,W) = \prod_{\alpha\in T}\left[\left(\frac{f_\alpha}{\pi}\right)^{\frac{N_\alpha}{2}} e^{-f_\alpha \sum_{i\in\alpha} w_{a_{\alpha,i}} w_{s_{\alpha,i}}}\right], \tag{35}$$

where I is the image; α indexes the subbands of T; f_α is the value of f on subband α; i indexes the wavelets within each subband; $w_{a_{i,\alpha}}$ and $w_{s_{i,\alpha}}$ are the (α, i) coeff cients using the primal and dual wavelet bases from the primal ($|a\rangle$) and dual ($|s\rangle$) wavelets, respectively; and N_α is the number of pixels in the subband α. Refer to section 2.2 for the relationship between the lifting weights $W = (p_j, u_j)$ and the primal-dual wavelet pair ($|a\rangle, |s\rangle$).

4.1.1 Parameter Estimation

MAP estimates of the parameters for a given texture are found by examining the probability of the parameters given a set of images $d = \{I_n\}$ of the texture:

$$\Pr(f,T,W|d) \propto \Pr(d|f,T,W)\Pr(f|T,W)\Pr(T|W)\Pr(W) \tag{36}$$

We choose the prior probabilities $\Pr(f|T,W)$ and $\Pr(T|W)$ as the same way as we did for $\Pr(f|T)$ and $\Pr(T)$ in equation (31) in the previous section. We choose the wavelet prior $\Pr(W)$ to be uniform.

As in the previous section, differentiating (35) with respect to f_α gives us the MAP estimate of f for fixed T and W:

$$\hat{f}_\alpha = \frac{N_\alpha}{2\sum_{i\in\alpha}|w_{a_{i,\alpha}} w_{s_{i,\alpha}}|} \tag{37}$$

A depth-first search through the space of dyadic decompositions allows us to find the MAP estimate for T efficiently for a fixed wavelet choice W.

Finally the MAP estimate for W is found as follows:

$$\hat{W} = \underset{(x\in P, y\in U)}{\arg\max} \Pr(d|f, T, W_{x,y}), \tag{38}$$

where P and U are the sets of choices for the lifting weights p and u.

4.1.2 Classification

We consider the approximation $\Pr(I_R|f, T, W)$ to the exact probability distribution for the texture on a region R as in equation (33) and follow the same classification procedure as used in section 3.3.

4.2 Experimental Results

In this section, we evaluate the proposed model by focusing on finding the optimal mother wavelet for a given texture from a finite set of mother wavelet choices. We show an example using interpolating wavelets with P and U filters of length 4. In general, one can define the interpolating filter template of length 4, denoted Int_4, by

$$\text{Int}_4 = \begin{pmatrix} -v & \frac{1}{2}+v & \frac{1}{2}+v & -v \end{pmatrix}$$

We choose $v = (k-1)/64$ for $k \in [1, 2, \ldots, 17]$. The resulting interpolation functions are shown in table 4.

The choices 1 and 5 correspond to the classical linear and cubic interpolation functions, respectively. We define a set of interpolating wavelets by choosing the interpolating templates in the table as P and U filters. We denote such wavelets (k-l), where k and l are the indices for the chosen P and U filters, respectively. For example, the well-known biorthogonal wavelets (2,2), (4,2), (2,4) and (4,4) (using the vanishing moment pair notation) correspond to the wavelet choices (1-1), (5-1), (1-5) and (5-5) in the table.

4.2.1 Parameter Estimation

We use the same textures and mosaics used in sections 3.4.1 and 3.4.2, respectively. We compute $\Pr(d|\hat{f}, \hat{T}, (P, U))$ for each of the mother wavelet choices (k-l) using the 17 interpolating functions shown in table 4. This yields 289 choices of mother wavelet filters to be used in parameter estimation experiments. In Figure 4, we show the logarithms of the probabilities for the different (k-l) mother wavelets choices for the textures Raffia, Herring, Wool and Grass (brightness is proportional to the log probability).

k	Int_4
1	$\begin{pmatrix} 0 & \frac{1}{2} & \frac{1}{2} & 0 \end{pmatrix}$
2	$\begin{pmatrix} -\frac{1}{64} & \frac{33}{64} & \frac{33}{64} & -\frac{1}{64} \end{pmatrix}$
3	$\begin{pmatrix} -\frac{1}{32} & \frac{17}{32} & \frac{17}{32} & -\frac{1}{32} \end{pmatrix}$
4	$\begin{pmatrix} -\frac{3}{64} & \frac{35}{64} & \frac{35}{64} & -\frac{3}{64} \end{pmatrix}$
5	$\begin{pmatrix} -\frac{1}{16} & \frac{9}{16} & \frac{9}{16} & -\frac{1}{16} \end{pmatrix}$
6	$\begin{pmatrix} -\frac{5}{64} & \frac{37}{64} & \frac{37}{64} & -\frac{5}{64} \end{pmatrix}$
7	$\begin{pmatrix} -\frac{3}{32} & \frac{19}{32} & \frac{19}{32} & -\frac{3}{32} \end{pmatrix}$
8	$\begin{pmatrix} -\frac{7}{64} & \frac{39}{64} & \frac{39}{64} & -\frac{7}{64} \end{pmatrix}$
9	$\begin{pmatrix} -\frac{1}{8} & \frac{5}{8} & \frac{5}{8} & -\frac{1}{8} \end{pmatrix}$
10	$\begin{pmatrix} -\frac{9}{64} & \frac{41}{64} & \frac{41}{64} & -\frac{9}{64} \end{pmatrix}$
11	$\begin{pmatrix} -\frac{5}{32} & \frac{21}{32} & \frac{21}{32} & -\frac{5}{32} \end{pmatrix}$
12	$\begin{pmatrix} -\frac{11}{64} & \frac{43}{64} & \frac{43}{64} & -\frac{11}{64} \end{pmatrix}$
13	$\begin{pmatrix} -\frac{3}{16} & \frac{11}{16} & \frac{11}{16} & -\frac{3}{16} \end{pmatrix}$
14	$\begin{pmatrix} -\frac{13}{64} & \frac{45}{64} & \frac{45}{64} & -\frac{13}{64} \end{pmatrix}$
15	$\begin{pmatrix} -\frac{7}{32} & \frac{23}{32} & \frac{23}{32} & -\frac{7}{32} \end{pmatrix}$
16	$\begin{pmatrix} -\frac{15}{64} & \frac{47}{64} & \frac{47}{64} & -\frac{15}{64} \end{pmatrix}$
17	$\begin{pmatrix} -\frac{1}{4} & \frac{3}{4} & \frac{3}{4} & -\frac{1}{4} \end{pmatrix}$

Table 4: Different choices for length 4 interpolation function templates.

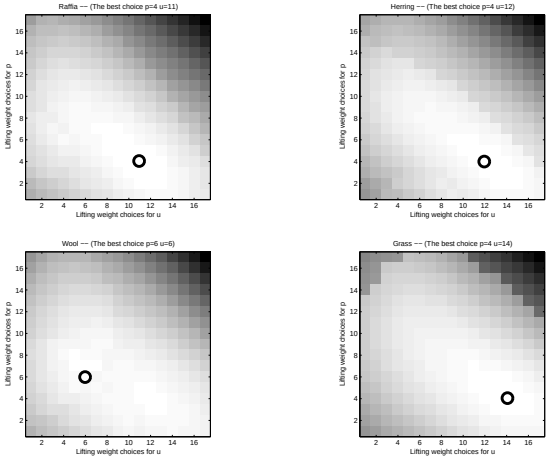

Figure 4: Log probabilities for different choices of P and U lifting weights for different textures. Increasing brightness corresponds to increasing probability. Top row: Raffia ($\hat{W}$ = (4-11)) and Herring ($\hat{W}$ = (4-12)); Bottom Row: Wool ($\hat{W}$ = (6-6)) and Grass ($\hat{W}$ = (4-14)).

The optimal mother wavelets $\hat{W}$ for each of the test textures were found to be (4-11), (4-12), (6-6) and (4-14), respectively. Interestingly, none of the above choices corresponds to the commonly used wavelet filters. The parameters T and f are estimated as described earlier. They are shown graphically and compared with the corresponding power spectra in Figure 5. The brightness of each subband is proportional to $1/f_\alpha$.

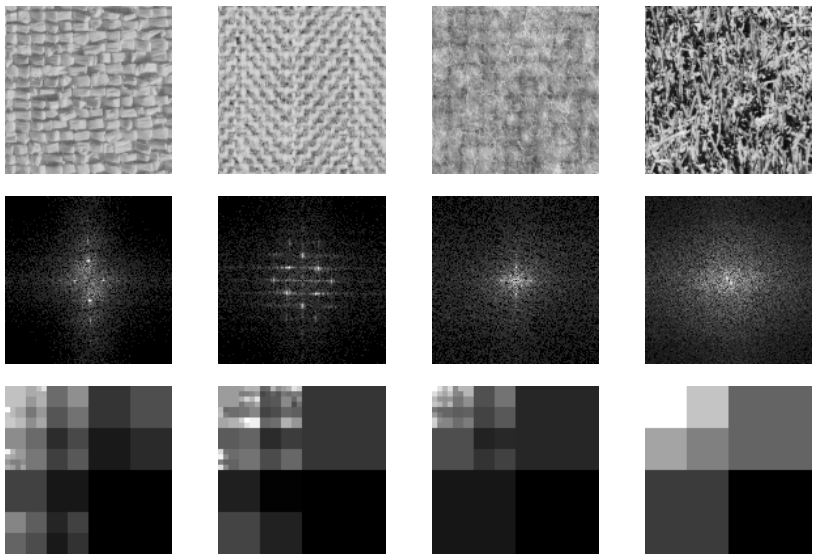

Figure 5: Parameter estimation. Row 1: textures Raffia, Herring, Wool, and Grass; row 2: their power spectra; row 3: their estimated parameters using the optimal mother wavelet.

4.2.2 Classification

We present the classification performance of the texture-adaptive optimal biorthogonal mother wavelet packet model using single texture images and texture mosaic images. Figure 6 shows the classification maps for four textures, classified using all four trained texture models on each of the single texture images. The percentages of misclassified pixels are listed in table 5. Similarly, Figure 7 shows the classification performance for test mosaics, M1, M2, M3 and M4, made of 4 test textures. The percentages of misclassified pixels are listed in table 6.

As can be seen from the tables, using the optimal mother wavelet for modelling the textures results in better classification performance than using fixed mother wavelets involving lifting templates of length 4, *i.e.,* (4,4), (4,2) and (2,4).

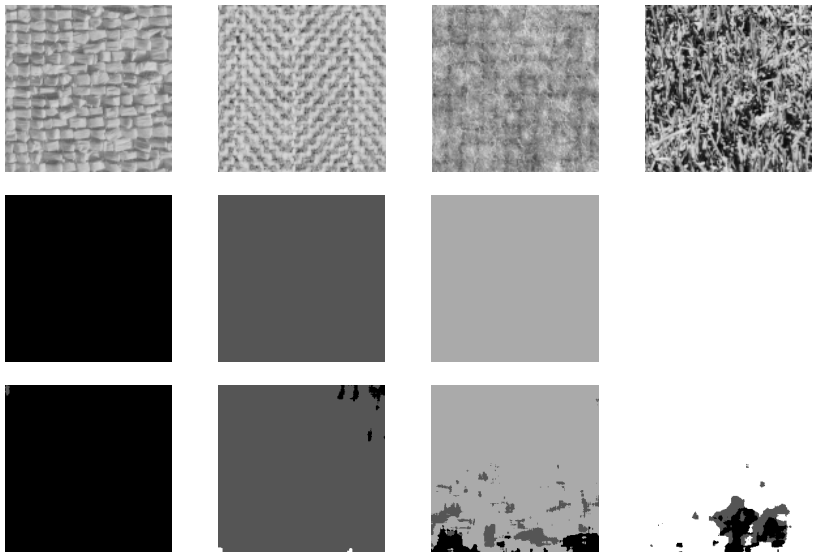

Figure 6: Classif cation results. Row 1: Raff a, Herring, Wool, and Grass; row 2: ground truth; rows 3: classif cation map using the optimal mother wavelet.

	T1	T2	T3	T4	Average
Optimal	0.13	1.41	9.21	9.98	5.18
(2,4)	0.19	1.79	13.11	11.91	6.75
(4,2)	0.01	4.80	7.16	11.97	5.98
(4,4)	0.18	1.89	15.49	10.02	6.90

Table 5: Percentages of misclassif ed pixels (Single textures).

	M1	M2	M3	M4	Average
Optimal	2.79	4.76	6.86	8.93	5.84
(2,4)	2.67	4.72	6.78	10.96	6.28
(4,2)	2.83	5.77	6.06	9.18	5.96
(4,4)	2.83	7.60	6.07	10.62	6.78

Table 6: Percentages of misclassif ed pixels (Mosaics).

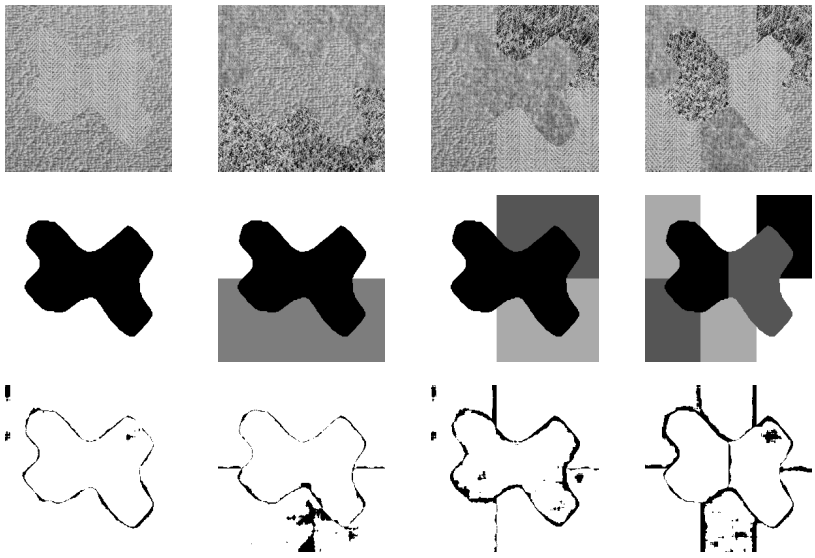

Figure 7: Classif cation results. Row 1: mosaics M1, M2, M3, and M4; row 2: ground truth; rows 3: misclassif ed pixels (in black) using the optimal mother wavelet.

4.3 Conclusions

In this section, we have incorporated the choice of mother wavelet into an adaptive probabilistic texture model based on biorthogonal wavelets. The optimal mother wavelet for a given texture is given by the mother wavelet that maximizes the MAP probability of the derived biorthogonal wavelet packet texture model. We have shown examples of the best choices for prediction and update lifting weights using length 4 lifting templates for four different textures. The optimal lifting weight choices result in better classif cation performance than the standard (4,4), (2,4) and (4,2) wavelets, all of which include length 4 prediction and/or update lifting templates.

5 Conclusions

In this report, we have presented an adaptive probabilistic texture model based on biorthogonal wavelets and used it for texture classification and analysis. We also included the mother wavelet as a parameter to this model, so that the optimal mother wavelet filter for a given texture can be used in the model. In this model, both the primal and the dual wavelets associated with a specific biorthogonal wavelet transform are used in the energy computation, in parameter estimation, and for classification.

For both orthogonal and biorthogonal wavelets, shorter wavelets with fewer vanishing moments classify better than longer wavelets with more vanishing moments. The biorthogonal wavelets (2,2) and (4,4) resulted in better classification results compared to the corresponding compactly supported orthogonal wavelets with the same number of vanishing moments, D4 and D8.

The optimal mother wavelets for textures obtained using the length four prediction and update lifting templates have shown better classification performances compared to those obtained using the fixed mother wavelets that use standard weights for length four prediction and/or update lifting templates. As shown in the examples, the optimal lifting weight choices for Int_4 class of wavelets result in better classification performance than the standard (4,4), (2,4) and (4,2) wavelets, all of which include length 4 prediction and/or update lifting templates.

The use of the lifting scheme in this model provides very fast computation, in both training and classification, and also a parameterization of the wavelet filters that we plan to use in future work to optimize the mother wavelet for a given texture using this model, in addition to spatial domain wavelet filter design.

References

[1] A. K. Jain and F. Farrokhnia, "Unsupervised texture segmentation using gabor f lters," *Pattern Recognition*, vol. 24, no. 12, pp. 1167–1186, 1991.

[2] G. M. Haley and B. S. Manjunath, "Rotation-invariant texture classif cation using a complete space-frequency model," *IEEE Trans. Image Processing*, vol. 8, no. 2, pp. 255–269, 1999.

[3] J. M. Coggins and A. K. Jain, "A spatial f tering approach to texture analysis," *Pattern Recognition Letters*, vol. 3, no. 3, pp. 195–203, 1985.

[4] T. Chang and C.-C. J. Kuo, "Texture analysis and classif cation with tree structured wavelet transform," *IEEE Trans. Image Processing*, vol. 2, no. 4, pp. 429–441, 1993.

[5] A. Laine and J. Fan, "Texture classif ction by wavelet packet signatures," *IEEE Trans. Patt. Anal. Mach. Intell.*, vol. 15, no. 11, pp. 1186–1190, 1993.

[6] K. Brady, I. H. Jermyn, and J. Zerubia, "Texture analysis: An adaptive probabilistic approach," in *Proc. IEEE ICIP*, vol. 2, 2003, pp. 1045–1048.

[7] ——, "A probabilistic framework for adaptive texture description," INRIA, Report 4920, Sep. 2003.

[8] N. Rajpoot, "Local discriminant wavelet packet basis for texture classif cation," in *Wavelets: Applications in Signal and Image Processing X*, vol. Proc. SPIE 5207, 2003, pp. 774–783.

[9] M. Acharyya and M. K. Kundu, "Adaptive basis selection for multi texture segmentation by m-band wavelet packet frames," in *Proc. IEEE ICIP*, vol. 1, 2001, pp. 622–625.

[10] M. Unser, "Texture classif cation and segmentation using wavelet frames," *IEEE Trans. Image Processing*, vol. 4, no. 11, pp. 1549–1560, 1995.

[11] G. V. de Wouwer, P. Scheunders, and D. V. Dyck, "Statistical texture characterization from discrete wavelet representation," *IEEE Trans. Image Processing*, vol. 8, no. 4, pp. 592–598, 1999.

[12] S. Liapis, N. Alvertos, and G. Tziritas, "Maximum likelihood texture classif cation and bayesian texture segmentation using discrete wavelet frames," in *Proc. IEEE Int'l conf. on Digital Signal Processing*, vol. 2, 1997, pp. 1107–1110.

[13] T. Randen and J. H. Husoy, "Filtering for texture classif cation: A comparative study," *IEEE Trans. Patt. Anal. Mach. Intell.*, vol. 21, no. 4, pp. 291–309, 1999.

[14] M. D. Adams and F. Kossentini, "Reversible integer-to-integer wavelet transforms for image compression: Performance evaluation and analysis," *IEEE Trans. Image Processing*, vol. 9, no. 6, pp. 1010–1024, 2000.

[15] D. M. R. A. Mojsilovic´, M. V. Popovic, "On the selection of an optimal wavelet basis for texture characterization," *IEEE Trans. Image Processing*, vol. 9, no. 12, pp. 2043–2050, 2000.

[16] T. Randen and J. H. Husoy, "Texture segmentation using f lters with optimized energy seperation," *IEEE Trans. Image Processing*, vol. 8, no. 4, pp. 571–582, 1999.

[17] ——, "Optimal f lter-bank design for multiple texture discrimination," in *Proc. IEEE ICIP*, vol. 2, 1997, pp. 215–218.

[18] F. Nergard and T. Randen, "Optimization of spatial f lters for image texture feature seperation by simulated annealing," in *NORSIG*, 1996, pp. 251–254.

[19] E. B. da Silva and M. Ghanbari, "On the performance of linear phase wavelet transforms in lowbit-rate image coding," *IEEE Trans. Image Processing*, vol. 5, no. 5, pp. 689–704, 1999.

[20] I. Daubechies and W. Sweldens, "Factoring wavelet transforms into lifting steps," *J. Fourier Anal. Appl.*, vol. 4, no. 3, pp. 245–267, 1998.

[21] W. Sweldens, "The lifting scheme: A new philosophy in biorthogonal wavelet constructions," in *Wavelet Applications in Signal and Image Processing III*, A. F. Laine and M. Unser, Eds., vol. Proc. SPIE 2569, 1995, pp. 68–79.

[22] G. Strang and T. Nguyen, *Wavelets and Filter Banks*, 2nd ed. Wellesley, MA: Wellesley-Cambridge Press, 1997.

[23] Y. Meyer and R. Ryan, *Wavelets: Algorithms and Applications*. Philadelphia, PA: Society for Industrial and Applied Mathematics, 1991.

[24] W. Sweldens, "Wavelets and the lifting scheme: A 5 minute tour," *Z. Angew. Math. Mech.*, vol. 76 (Suppl. 2), pp. 41–44, 1996.

[25] P. Brodatz, *Textures: A Photographic Album for Artists and Designers*. New York, USA: Dover, 1966.

Unité de recherche INRIA Sophia Antipolis
2004, route des Lucioles - BP 93 - 06902 Sophia Antipolis Cedex (France)

Unité de recherche INRIA Futurs : Parc Club Orsay Université - ZAC des Vignes
4, rue Jacques Monod - 91893 ORSAY Cedex (France)
Unité de recherche INRIA Lorraine : LORIA, Technopôle de Nancy-Brabois - Campus scientif que
615, rue du Jardin Botanique - BP 101 - 54602 Villers-lès-Nancy Cedex (France)
Unité de recherche INRIA Rennes : IRISA, Campus universitaire de Beaulieu - 35042 Rennes Cedex (France)
Unité de recherche INRIA Rhône-Alpes : 655, avenue de l'Europe - 38334 Montbonnot Saint-Ismier (France)
Unité de recherche INRIA Rocquencourt : Domaine de Voluceau - Rocquencourt - BP 105 - 78153 Le Chesnay Cedex (France)

Éditeur
INRIA - Domaine de Voluceau - Rocquencourt, BP 105 - 78153 Le Chesnay Cedex (France)
http://www.inria.fr
ISSN 0249-6399